Landslide Sensitivity and Response to Precipitation Changes in Wet and Dry Climates

Alexander L Handwerger[1], Eric J. Fielding[1], Simran Singh Sangha[2], and David Bekaert[3]

[1]Jet Propulsion Laboratory, Caltech
[2]Jet Propulsion Laboratory
[3]Jet Propulsion Lab

November 30, 2022

Abstract

Slow-moving landslides are hydrologically driven. Yet, landslide sensitivity to precipitation, and in particular, precipitation extremes, is difficult to constrain because landslides occur under diverse hydroclimatological conditions. Here we use standardized open-access satellite radar interferometry data to quantify the sensitivity of 38 landslides to both a record drought and extreme rainfall that occurred in California between 2015 and 2020. These landslides are hosted in similar rock types, but span more than ˜2 m/yr in mean annual rainfall. Despite the large differences in hydroclimate, we found these landslides exhibited surprisingly similar behaviors and hydrologic sensitivity, which was characterized by faster (slower) than average velocities during wetter (drier) than average years, once the impact of the drought diminished. Our findings may be representative of future landslide behaviors in California where precipitation extremes are predicted to become more frequent with climate change.

Hosted file

essoar.10510913.1.docx available at https://authorea.com/users/558298/articles/607573-landslide-sensitivity-and-response-to-precipitation-changes-in-wet-and-dry-climates

Landslide Sensitivity and Response to Precipitation Changes in Wet and Dry Climates

Alexander L. Handwerger[1,2], Eric J. Fielding[1], Simran S. Sangha[1,3], and David P.S. Bekaert[1]

[1]Jet Propulsion Laboratory, California Institute of Technology, Pasadena, USA.

[2]Joint Institute for Regional Earth System Science and Engineering, University of California, Los Angeles, Los Angeles, USA.

[3]Earth, Planetary, and Space Sciences, University of California, Los Angeles, CA, USA.

Corresponding author: Alexander L. Handwerger (alexander.handwerger@jpl.nasa.gov)

Key Points:

- Open-access standardized ARIA InSAR products can be used to identify and monitor landslides over large regions
- Slow-moving landslides occur in both dry and wet environments with mean annual rainfall ranging from ~200 to ~2000 mm/yr
- Landslides are sensitive to seasonal, annual, and multi-year changes in rainfall in both dry and wet environments.

Abstract

Slow-moving landslides are hydrologically driven. Yet, landslide sensitivity to precipitation, and in particular, precipitation extremes, is difficult to constrain because landslides occur under diverse hydroclimatological conditions. Here we use standardized open-access satellite radar interferometry data to quantify the sensitivity of 38 landslides to both a record drought and extreme rainfall that occurred in California between 2015 and 2020. These landslides are hosted in similar rock types, but span more than ~2 m/yr in mean annual rainfall. Despite the large differences in hydroclimate, we found these landslides exhibited surprisingly similar behaviors and hydrologic sensitivity, which was characterized by faster (slower) than average velocities during wetter (drier) than average years, once the impact of the drought diminished. Our findings may be representative of future landslide behaviors in California where precipitation extremes are predicted to become more frequent with climate change.

Plain Language Summary

Landslides are often triggered by precipitation and as a result are sensitive to local climate conditions. Climate change is impacting precipitation patterns worldwide and therefore will likely have a profound influence on landslide activity over the coming decades. Here we use standardized open-access satellite radar data to assess landslide sensitivity to precipitation in California between 2015 and 2020. During this time period, California experienced some of the

wettest and driest years on record, which is a precipitation pattern that is predicted to become the norm over the next century in California. We found that landslides in both dry and wet regions of California were similarly sensitive to seasonal and multi-year changes in precipitation. These landslides moved faster than average during wet years and slower than average during dry years. Our findings further confirm landslide sensitivity to climate change under diverse hydroclimate conditions and highlight the need to establish a long time series of landslide behaviors that can be used to better predict future landslide activity.

1 Introduction

A foundational paradigm in landslide science is that precipitation triggers landslides. Precipitation promotes slope instability as water flows through the ground and raises the water table, or creates perched water tables, and as a result, increases pore-water pressures, reduces the effective normal stress (normal stress minus pore-water pressure), and reduces the frictional strength of the hillslope (Bogaard & Greco, 2016; Terzaghi, 1951). Once a hillslope fails as a landslide it can accelerate rapidly and fail catastrophically (Iverson et al., 2015; Jibson, 2006; Shugar et al., 2021), move downslope slowly for years to hundreds of years (Mackey et al., 2009; Nereson & Finnegan, 2018; Rutter & Green, 2011), or move slowly for a period of time before stabilizing or failing catastrophically (Agliardi et al., 2020; Handwerger, Huang, et al., 2019; Iverson, 2005; Kilburn & Petley, 2003). These different behavioral modes have important consequences for hazard assessment because fast-moving landslides can move at rates up to tens of meters per second and can easily claim lives (Iverson et al., 2015; Shugar et al., 2021), while slow-moving landslides move at rates of meters per year or less and can damage infrastructure (Lacroix, Handwerger, et al., 2020; Merriam, 1960).

Persistently active slow-moving landslides are well-suited for exploring hydrologic controls on landslide motion because they are relatively easy to monitor (compared to landslides with catastrophic failures), occur in wet and dry environments around the world where water is delivered by rainfall (Bayer et al., 2018; Malet et al., 2002), snowmelt (Coe et al., 2003; Matsuura et al., 2008), or irrigation (Lacroix, Dehecq, et al., 2020; Merriam, 1960), and their motion is closely linked to local groundwater conditions (Corominas et al., 2005; Finnegan et al., 2021; Iverson & Major, 1987). Furthermore, the hydrologic controls on slow-moving landslides, via pore pressure changes, are akin to the hydrologic controls on faults (Bhattacharya & Viesca, 2019; Cappa et al., 2019), glaciers (Minchew & Meyer, 2020; Moon et al., 2014), and rock glaciers (Cicoira et al., 2019; Kenner et al., 2017), and therefore investigating these landslides allows us to better understand each system.

Previous investigations on the hydrologic controls on slow-moving landslides have shown that precipitation causes slow-moving landslides to accelerate once the pore-water pressures have increased to sufficient levels in the landslide body and decelerate when the pore-water pressures drop (Finnegan et al., 2021; Iverson & Major, 1987; Malet et al., 2002). Thus, slow-moving landslides can slow

down or stop moving during dry periods, and speed up, reactivate, or fail catastrophically during wet periods (Bennett, Roering, et al., 2016; Handwerger, Fielding, et al., 2019; McSaveney & Griffiths, 1987; Nereson & Finnegan, 2018). The hydrologic response of landslides can also be size-dependent where larger and thicker landslides are somewhat less sensitive to daily to annual changes in rainfall compared to smaller and thinner landslides that typically experience greater swings in pore-water pressure (Bennett, Roering, et al., 2016; Handwerger, Fielding, et al., 2019). Indeed, this is an expected consequence of pore water transmission in saturated ground (Iverson and Major, 1987). However, recent work by Finnegan et al. (2021) shows nearly instantaneous pore pressure transmission to depth once the vadose zone of the Oak Ridge landslide, California becomes saturated each year, which suggests vadose zone thickness, rather than total landslide thickness, may be the relevant length scale controlling the landslide response in settings where the surface of a landslide becomes unsaturated, for example in locations with highly seasonal rainfall delivery. Nonetheless, both climate and landslide size may govern the hydrologic sensitivity of landslides.

Satellite-based interferometric synthetic aperture radar (InSAR) data can be analyzed alongside precipitation and groundwater data and used to inventory and monitor landslides with the high spatial and temporal resolution necessary to explore hydrologic controls on landslide motion (Bayer et al., 2018; Cohen-Waeber et al., 2018; Handwerger et al., 2013). The open-access data collected by Copernicus Sentinel-1 A/B satellites, in particular, has revolutionized InSAR studies on landslides (Bayer et al., 2018; Carlà et al., 2019; Handwerger, Huang, et al., 2019; Intrieri et al., 2017; Liu et al., 2021; Raspini et al., 2018), and other ground surface deformation (Cigna & Tapete, 2021; Huang et al., 2017; Lundgren et al., 2020; Strozzi et al., 2020), and has led to the development of automated InSAR processing systems that produce derived standard products that can be used for scientific research (Buzzanga et al., 2020; Dehls et al., 2019; Jones et al., 2021; Lazecký et al., 2020). These derived standard products will become especially important as the volume of InSAR data continues to grow, making it increasingly challenging to process and download InSAR data for large regions on a personal computer. Furthermore, the recent push to provide open-access standardized InSAR products, along with a suite of tools to analyze these data (e.g., Morishita et al., 2020; Yunjun et al., 2019), increases data accessibility to the broader geoscience community, which will undoubtedly lead to major scientific advances.

In this study we analyze open-access standardized Sentinel-1 interferograms automatically processed by the JPL-Caltech Advanced Rapid Imaging and Analysis (ARIA) Center for Natural Hazards project (Bekaert et al., 2019) to identify and monitor landslides in both wet and dry climates in California, USA. California has a large quantity of active slow-moving landslides and has been a major focus area for landslide investigations for decades (Iverson & Major, 1987; Keefer & Johnson, 1983; Kelsey, 1978; Merriam, 1960). Slow-moving landslides in California exhibit distinct seasonal kinematic patterns (Cohen-Waeber et al., 2018;

Finnegan et al., 2021; Handwerger et al., 2013; Iverson & Major, 1987) that are a consequence of the regions Mediterranean climate with mild wet winters and hot dry summers, and multi-year kinematic changes that result from precipitation deficits or surplus (Bennett, Roering, et al., 2016; Booth et al., 2020; Mackey et al., 2009; Nereson & Finnegan, 2018). California also has a large rainfall gradient from north to south and west to east, with parts of northern California receiving $>$ 3000 mm/yr of rainfall and parts of southern California receiving $<$ 200 mm/yr (Figure 1a). There are slow-moving landslides in both wet and dry regions of California, which presents an opportunity to examine how variability in hydroclimatology controls landslide behaviors.

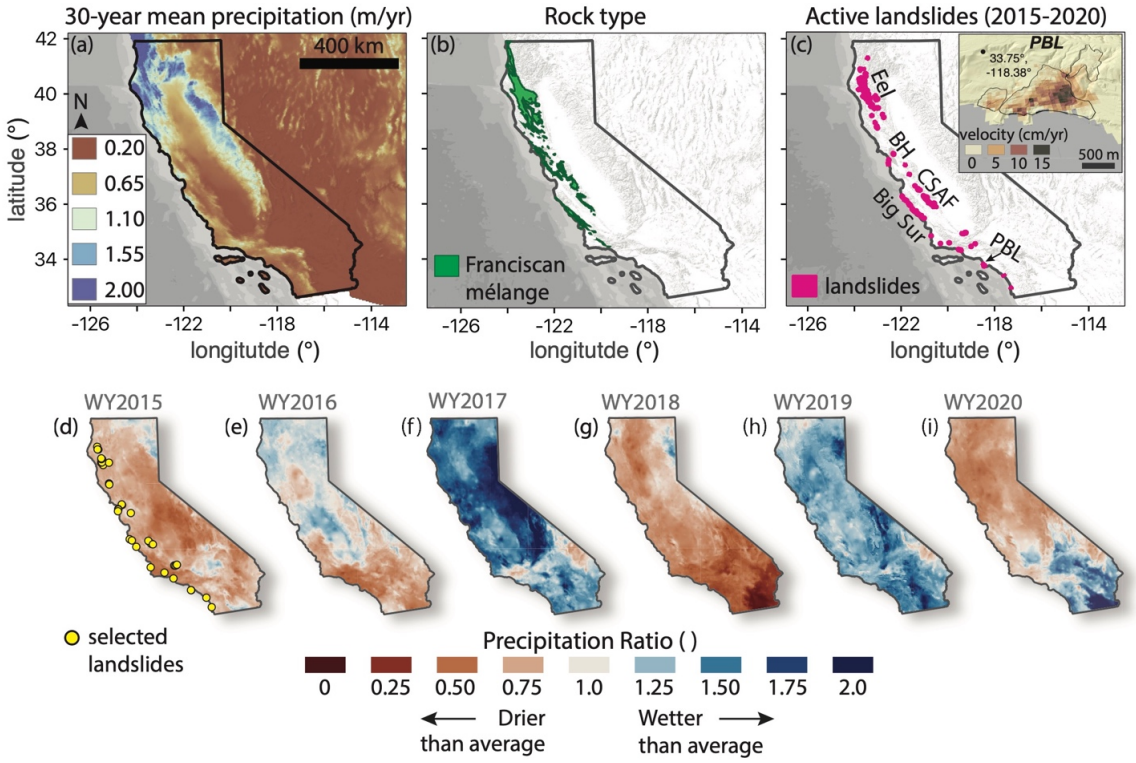

Figure 1. Maps of precipitation, rock type, and landslide locations. (a) 30-year mean water year precipitation (m/yr) with period WY1990-WY2019 calculated from PRISM data. (b) Simplified geologic map showing the areal extent of the Franciscan mélange rock unit. (c) Location of active landslides identified with our InSAR analyses. Well-studied landslide groups labeled Eel = Eel River, BH = Berkeley Hills, CSAF = Central San Andreas Fault, PBL = Portuguese Bend landslide. Inset shows oblique view of InSAR velocity map for Portuguese Bend landslide (PBL) draped over a lidar hillshade. Black circle shows the location of the reference point for the time series and black polygons show active landslide boundaries.

(d-i) Precipitation Ratio (total WY precipitation / 30-year mean precipitation) for WY2015-WY2020. Red colors correspond to drier than average years and blue colors correspond to wetter than average years. Yellow circles in (d) show landslides selected for detailed time series analyses.

We focus our study between the 2015 and 2020 water years (WY), during which California experienced extreme changes in rainfall (Figure 1d-i and Figure S1). WY2015 and WY2016 were the last two years of a historic drought, which was one of the most severe for hundreds of years (Robeson, 2015; Swain et al., 2014). The drought officially ended in WY2017, which was an extremely wet year across most of California, and was the second wettest year on record in places (Swain et al., 2018; Wang et al., 2017). There were many landslides that were triggered or accelerated and reactivated in WY2017 (Finnegan et al., 2021; Handwerger, Fielding, et al., 2019), including the catastrophic Mud Creek landslide that destroyed State Highway 1 (Handwerger, Huang, et al., 2019; Jacquemart & Tiampo, 2021; Warrick et al., 2019). Dry conditions returned in WY2018 due to below average rainfall, followed by wet conditions in WY2019 due to above average rainfall, and finally a return to dry conditions in WY2020 due to below average rainfall. These back and forth changes from dry to wet conditions are consistent with long-term climate predictions and therefore may be representative of climate patterns in California over the next century (Polade et al., 2017; Swain et al., 2018).

2 Data and Methods

2.1 Interferometric Synthetic Aperture Radar Processing and Analysis

Open-access SAR data from the C-band (~5.6 cm radar wavelength) Copernicus Sentinel-1 A/B satellites were automatically processed to standardized interferograms by the ARIA project (Bekaert et al., 2019). ARIA uses the open-access JPL InSAR Scientific Computing Environment (ISCE) software to process the interferograms (Rosen et al., 2012). These standardized interferograms are corrected for topographic contributions to phase and geocoded to a ~90 m (3 arc second) pixel spacing using the Shuttle Radar Topography Mission (SRTM) digital elevation model (DEM) (Farr et al., 2007). ARIA provides key data needed for deformation analyses and time series inversions including geocoded unwrapped interferograms, coherence, incidence and azimuth angles, and the SRTM DEM and water mask.

We used the ARIA-tools open-source package in Python (Buzzanga et al., 2020) to download and prepare 1689 interferograms covering California (Table S1). We inverted the interferograms to deformation time series using the Miami InSAR Time-series software in PYthon (MintPy) (Yunjun et al., 2019). We set the maximum number of connected neighbors = 2 to remove longer time span interferograms that often have low coherence and are more likely to contain unwrapping errors for persistently moving features such as slow-moving landslides (e.g., Handwerger, Huang, et al., 2019). We quantified InSAR uncertainty using a bootstrapping technique (Efron & Tibshirani, 1986; Bekaert et al., 2020)

with 400 iterations for each time series. More information on the InSAR data processing can be found in the Supporting Information.

2.2 Landslide Reconnaissance

We identified active landslides by examining the time-averaged InSAR velocity maps. Active slow-moving landslides displayed localized deformation zones with relatively high velocity (Figures 1c inset). We then confirmed true landslides using DEMs, Google Earth imagery, and previously published landslide inventories. We began our landslide identification by examining the InSAR velocity in well-known landslide areas in northern California (Bennett, Miller, et al., 2016; Handwerger, Fielding, et al., 2019), central California (Booth et al., 2020; Cohen-Waeber et al., 2018; Finnegan et al., 2019; Scheingross et al., 2013; Wills et al., 2001), and southern California (Calabro et al., 2010; Jibson, 2006; Merriam, 1960; Swirad & Young, 2021; Young, 2015). We also examined landslide areas documented in the California Geologic Survey statewide landslide inventory (Wills et al., 2017). After examining these known landslide areas, we then systematically expanded outward from these regions to identify active landslides in all mountainous regions of California. We quantified landslide metrics such as area, length, width, and slope angle using the SRTM ~30 m (1 arc second) DEM. We classified the active landslide types as slumps, earthflows, and complexes and estimated landslide volume and thickness using geometric scaling relations for slow-moving landslides in California (see Supporting Information).

To further assess the kinematic behavior of the slow-moving landslides in wet and dry environments during wet and dry years, we selected a subset of landslides to perform detailed time series investigation (Figure 1d). These landslides were selected based on their relatively high velocity signal (i.e., strong InSAR signal) and their location within California's different hydroclimatic regimes. We characterized the landslide motion by calculating the spatial mean of the fastest moving kinematic zone and used a moving median temporal smoothing filter to further reduce noise and highlight the seasonal and annual deformation signals (Figures S2 and S3). We explored environmental controls on landslides by examining the rock type and precipitation data in active landslide areas. Rock type data are provided by the California Geologic Survey (Jennings et al., 2010) and precipitation data are provided by the Parameter-elevation Regressions on Independent Slopes Model (PRISM) (see Data Availability). We then quantified landslide sensitivity to rainfall by exploring relative changes in precipitation and landslide velocity. To explore relative changes in precipitation and velocity, we defined the Precipitation Ratio as the total water year precipitation divided by the 30-year mean water year precipitation (calculated from WY1990-WY2019) at each landslide (Figure 1d-i), and the Velocity Ratio as the water year velocity divided by the average velocity from WY2016-WY2019.

3 Results

3.1 Landslide Inventory

We manually identified and mapped 247 active slow-moving landslides in Cal-

ifornia (Figure 1c). Many, if not all of these landslides have been previously identified by other studies (Bennett, Miller, et al., 2016; Cohen-Waeber et al., 2018; Finnegan et al., 2019; Handwerger, Fielding, et al., 2019; Jibson, 2006; Merriam, 1960; Scheingross et al., 2013; Swirad & Young, 2021; Wills et al., 2001). These landslides consisted of different types including 71 slumps, 72 earthflows, and 104 landslide complexes (Table S2). As an expected consequence of the relatively coarse resolution (90 m pixel spacing) of the ARIA standardized InSAR product, we identified mostly larger landslides with areas ranging from 0.018 to 11 km^2 with a mean area of 0.5 km^2 (Table S2). The active landslides are distributed throughout the mountainous regions in western California, with the vast majority (230 of 247) in the Coast Ranges, and they spanned nearly the entire latitudinal extent of the state. Regions with the highest density of landslides include the well-known landslide hotspots such as the Eel River catchment, Big Sur coast, and Central San Andreas Fault (Figure 1c). There are also landslides located in populated and highly traveled zones such as Los Angeles and Berkeley, and along California State Highway 1 and State Highway 101 and thus pose a threat to infrastructure and life. Although we identified a large quantity of landslides, our inventory is an underestimate of the true landslide activity in California for three main reasons; 1) we were unable to identify landslides in regions with high seasonal snow cover (e.g., Sierra Nevada Mountains). To better explore regions with seasonal snow requires a different InSAR processing strategy that only utilizes data from snow-free periods. 2) The coarse resolution prevents us from imaging many of the smaller landslides that have been identified with higher resolution InSAR or field data (e.g., Scheingross et al., 2013; Nereson and Finnegan, 2018; Schulz et al., 2018; Handwerger, Fielding, et al., 2019). And 3) InSAR provides a 1D measurement and cannot detect landslide motion in the direction of the satellite heading (i.e., observational bias).

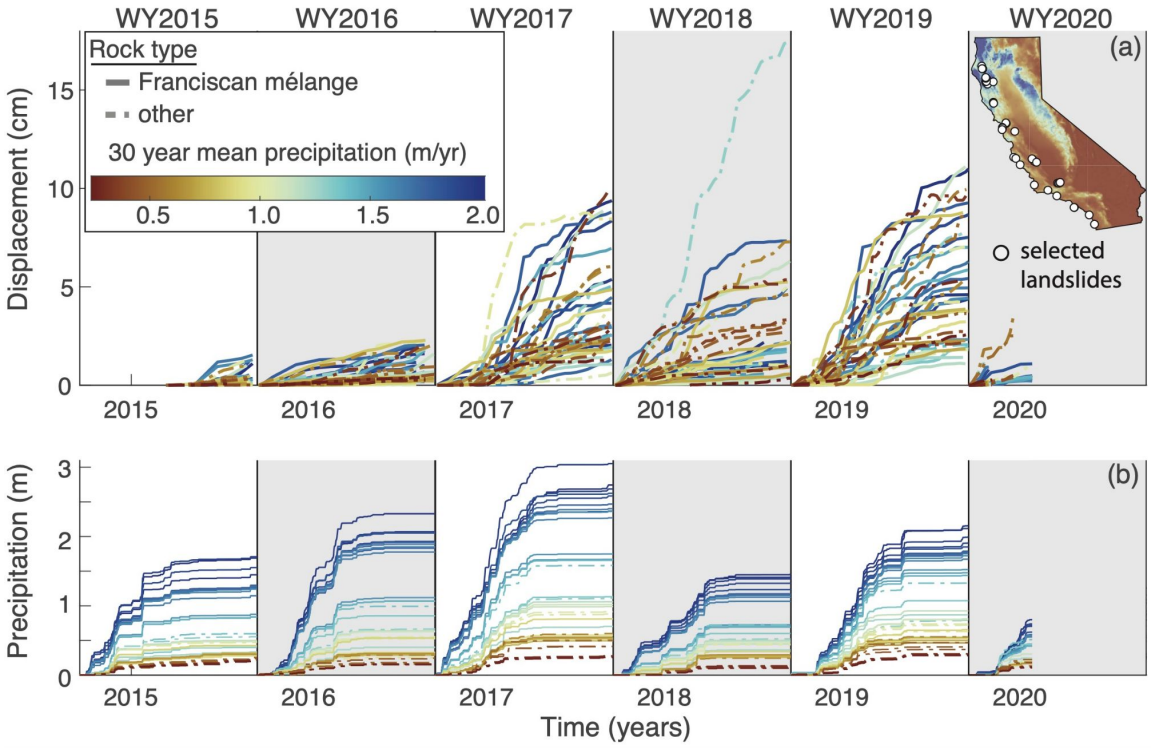

Figure 2. Landslide and precipitation time series for selected landslides in California. (a) Cumulative displacement time series projected onto the downslope direction and separated by water year (WY). The time series for each landslide are smoothed using a moving median temporal filter. Solid lines correspond to landslides occurring within the Franciscan mélange rock unit. Colors correspond to 30-year mean water year precipitation (WY1990-WY2019) for each landslide. Inset shows the location of the selected landslides on the 30-year mean precipitation map. (b) Cumulative precipitation time series for each landslide separated by WY and colored by 30-year mean water year precipitation.

Despite the large variability in rock type throughout California (Figure S4), we found that 228 of 247 landslides occurred in host rocks broadly defined as marine and nonmarine sedimentary or metasedimentary rock units (Figure S4 and Table S2). Of these landslides, 176 (71% of total) landslides are hosted within the Franciscan complex mélange (Figure 1b), which indicates a strong lithologic control on the distribution of slow-moving landslides. Numerous recent studies have made similar findings indicating that rock type exerts a primary control on slow-moving landslides in California (Bennett, Miller, et al., 2016; Handwerger, Fielding, et al., 2019; Scheingross et al., 2013; Xu et al., 2021) and throughout the world (see refs. in Lacroix, Handwerger, et al., 2020).

Estimates of precipitation from PRISM data showed that active landslides are occurring in both wet and dry environments (Figure 1). We found more than an order of magnitude precipitation variation between the wettest active landslide in northern California (30-year mean = 2180 mm/yr) and driest landslide in southern California (30-year mean = 216 mm/yr) (Figure 1a).

3.2 Seasonal and Annual Landslide Behavior

To assess the behavior of landslides occurring in wet and dry climates, we selected a subset of 38 landslides spanning more than an order of magnitude in 30-year mean precipitation (Figure 2 and Table S3). The subset of landslides consisted of different landslide types, rock types, and occurred in different environments including coastal and inland regions, as well as developed and undeveloped areas.

Annual downslope velocities ($\pm$ bootstrap uncertainty) averaged over the full study period ranged from 0.85 ± 0.56 to 9.7 ± 1.2 cm/yr (Table S3). Landslides occurring in both wet and dry regions of California exhibited seasonal kinematic changes in response to seasonal precipitation each year (Figure 2). Each landslide accelerated in response to infiltrating rainfall during the wet season before decelerating back to lower rates, or completely stopping, during the dry season.

The landslides also responded to changes in seasonal rainfall each year. We found large changes in seasonal precipitation caused large changes in displacement (Figures 2 and 3). There is no clear relationship between velocity, precipitation, and landslide size (Figures 3 and S5). We did find, however, that in general, the landslides moved faster than average during the wetter WY2017 and WY2019, and slower than average during the drier WY2016 and WY2018 (Figure 3). Interestingly, we observed the largest displacement at a single landslide during the drier than average WY2018 (Figure 2). This landslide is located on the coast and is thus likely subject to other driving forces such as debuttressing from wave erosion at its toe (see location of landslide 22 in Table S3).

Landslide sensitivity to precipitation also appeared to change during the study period. For instance, WY2016, which was the final year of the historic California drought, had both wetter and drier than average conditions in certain places, however all of the landslides were moving slower than average (velocity ratio < 1). WY2018 was drier than WY2016 across California, but a few landslides exhibited velocity ratios > 1. Our findings suggest that antecedent rainfall from the previous wet seasons, particularly the lingering impact of long-term droughts, likely play an important control on landslide behavior and sensitivity to rainfall.

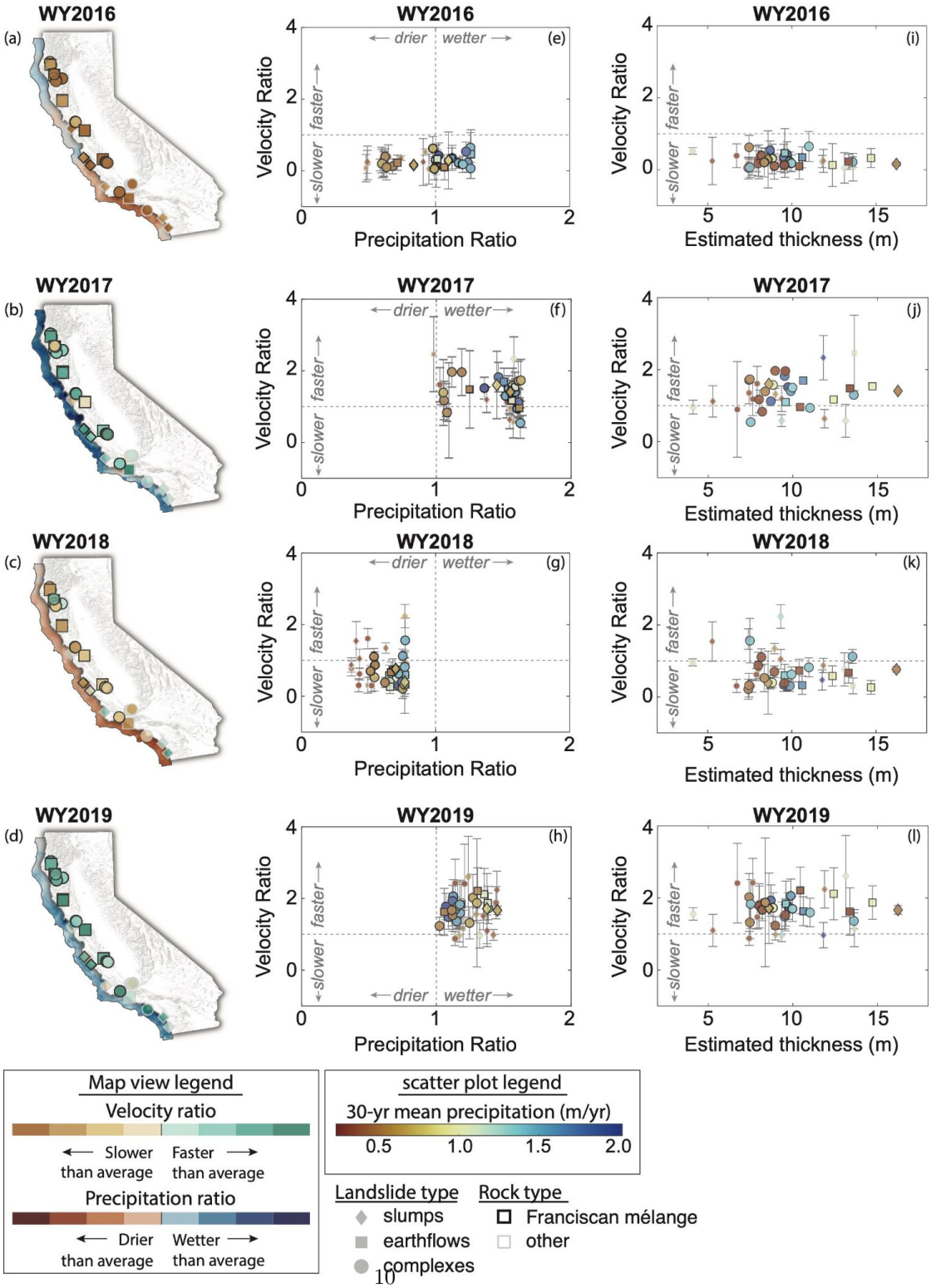
WY2016
(a)
WY2016
(e)
drier
wetter
faster
slower
Velocity Ratio
Precipitation Ratio
WY2016
(i)
Estimated thickness (m)
WY2017
(b)
WY2017
(f)
WY2017
(j)
WY2018
(c)
WY2018
(g)
WY2018
(k)
WY2019
(d)
WY2019
(h)
WY2019
(l)
Map view legend
Velocity ratio
Slower than average
Faster than average
Precipitation ratio
Drier than average
Wetter than average
scatter plot legend
30-yr mean precipitation (m/yr)
0.5
1.0
1.5
2.0
Landslide type
slumps
earthflows
complexes
Rock type
Franciscan mélange
other

Figure 3. Landslide response to changes in precipitation. (a-d) Maps of velocity and precipitation ratio by water year. Brown to green colors correspond to velocity ratio values for each landslide. Red to blue colors in background correspond to precipitation ratio. Symbols correspond to landslide type. Rock type is shown by black or gray symbol border color. (e-h) Velocity ratio as a function of precipitation ratio for selected landslides. (i-l) Velocity ratio as a function of estimated landslide thickness. Error bars show the uncertainty in the velocity ratio. Red to blue colors correspond to the 30-year mean water year precipitation (WY1990-WY2019) for each landslide. Symbols correspond to landslide type. Rock type is shown by black or gray symbol border color. We calculated the velocity ratio uncertainty using standard error propagation and assumed nil uncertainty in the precipitation data.

4 Discussion and Conclusion

Our study documents the first application of open-access standardized InSAR products from JPL ARIA to identify and monitor landslides across large regions. Although the coarse resolution InSAR product limits our ability to detect smaller landslides, it still provides valuable data that can be used to better understand landslide processes. Due to the large volume of open-access InSAR data that is currently available, and will continue to increase with time, especially with the upcoming launch of the NASA-ISRO SAR (NISAR) satellite, standardized InSAR products will become one of the primary ways to deliver InSAR data to the broader scientific community. The JPL Observation Products for End-Users from Remote Sensing Analysis (OPERA) project will soon be generating an operational high resolution displacement timeseries from Sentinel-1 and NISAR data over North America. With a spatial resolution of 30 m or better this product will be well-suited for identifying and monitoring landslides. Thus, it is important to continue to explore new approaches to analyze these InSAR products for scientific research, including use of automated or semi-automated detection and mapping techniques (e.g., Amatya et al., 2021; Milillo et al., 2021) .

Active slow-moving landslides across California occur in both dry and wet environments. Despite more than an order of magnitude difference in mean annual rainfall, these landslides exhibit similar first order behaviors in that they display seasonal and annual changes in displacement that correspond to local changes in rainfall, and are sensitive to seasonal, annual, and multi-annual changes in rainfall. Interestingly, we did not observe a strong climate- or size-dependent control on the kinematic response of these landslides. While size-dependent hydrologic sensitivity may be more obvious at the smaller regional scale (e.g., Bennett, Roering, et al., 2016; Handwerger, Fielding, et al., 2019), it appears to be less significant for these 38 landslides (Figure 2 and 3), which may have more variability in local conditions. Additionally, the landslides in dry and wet climates appear similarly sensitive to year-to-year changes in rainfall. One explanation for landslide sensitivity that is climate- and size-independent is that these persistently active landslides all maintain sufficiently high groundwater

levels that keep the landslides close to an acceleration threshold. Prior work on active slow-moving landslides has shown that these types of landslides typically have high groundwater levels year round and become effectively saturated during the wet season (Finnegan et al., 2021; Iverson & Major, 1987; Schulz et al., 2018). The ability to maintain high groundwater levels is possibly a consequence of rock type-controlled critical zone structure. Hahm et al. (2019) showed that the critical zone of the Franciscan mélange rock type, which is the predominant rock type of the landslides in our inventory, is characterized by a thin (< 3 m) seasonally unsaturated zone that becomes effectively saturated after a ~100 to 200 mm of seasonal rainfall at their field site in a wet region of northern California (mean annual rainfall ~1800 mm/yr). Similarly, Finnegan et al. (2021), showed that the Oak Ridge landslide, which occurs in an area of moderate rainfall in central California (mean annual rainfall ~640 mm/yr), becomes effectively saturated after about ~200 mm of seasonal rainfall. While not all of the landslides in our study occur in the Franciscan mélange, the other rock types are mostly marine and nonmarine sedimentary rocks that may bare similarity to the Franciscan mélange, and therefore may have a similar critical zone structure. Additionally, the landslides themselves may create an environment that allows them to retain water due to low permeability shear zones that inhibit water flow out of the landslide (Baum & Reid, 2000; Nereson et al., 2018). Thus, a thin seasonally unsaturated zone means that landslides in both the wetter and drier parts of the state can reach saturation during years with even modest rainfall. Once saturation occurs, excess precipitation should be shed as overland flow (e.g., Hahm et al., 2019) which may explain why landslides exhibit a relatively muted response to large differences in rainfall across the state.

Our study revealed that active slow-moving landslides moved seasonally during both dry and wet years and in dry and wet climates, indicating that even during dry periods and at dry landslides, there is still sufficient water input to maintain downslope motion for many landslides. Climate models predict that rainfall in California is likely to become more seasonal (i.e., a higher proportion of rainfall delivered in December to March) and dry to wet year extremes will become more common (Dong et al., 2019; Polade et al., 2017; Swain et al., 2018). Therefore, our study period may be representative of future precipitation and landslide behavioral patterns throughout California. While we currently cannot reliably predict landslide motion due to complex nonlinear relationships between precipitation, pore-water pressure, and velocity (e.g., Carey et al., 2019; Finnegan et al., 2021; Malet et al., 2002), we may be able to predict relative changes in landslide velocity in response to relative changes in precipitation. Therefore, it is necessary to continue to document landslide behaviors during 'normal' years that may serve as baselines for comparison and prediction of future landslide behaviors.

Acknowledgments

The authors thank Noah Finnegan for insightful discussions and comments

that helped improve our manuscript. We acknowledge ESA for providing the Sentinel-1 images through the Alaska Satellite Facility (ASF) for free, and ARIA for processing the InSAR data and ASF for providing open and free access to the standard InSAR displacement products. This work contains modified Copernicus data from the Sentinel-1A and 1B satellites provided by the ESA. Part of this research was carried out at the Jet Propulsion Laboratory, California Institute of Technology, under a contract with the National Aeronautics and Space Administration (80NM0018D0004).

Data and Software Availability Statement

ARIA standard products were downloaded from the ASF Distributed Active Archive Centers (DAAC) using ARIA-tools available at https://github.com/aria-tools/ARIA-tools. The full list of interferograms used are shown in Table S1. Precipitation data is provided by Parameter-elevation Regressions on Independent Slopes Model (PRISM) available at https://prism.oregonstate.edu/. Precipitation time series for each landslide is taken at the centroid location listed in Table S3. The Miami INsar Time-series software in PYthon (MintPy) is available at https://github.com/insarlab/MintPy. Shuttle Radar Topography Mission (SRTM) DEMS are available at https://www.usgs.gov/centers/eros. Lidar digital elevation models are provided by OpenTopography and may be downloaded online (http://www.opentopography.org).

References

Agliardi, F., Scuderi, M. M., Fusi, N., & Collettini, C. (2020). Slow-to-fast transition of giant creeping rockslides modulated by undrained loading in basal shear zones. *Nature Communications*, *11*(1), 1–11.

Amatya, P., Kirschbaum, D., Stanley, T., & Tanyas, H. (2021). Landslide mapping using object-based image analysis and open source tools. *Engineering Geology*, *282*, 106000.

Baum, R., & Reid, M. (2000). Ground water isolation by low-permeability clays in landslide shear zones. *Landslides in Research, Theory and Practice. Thomas Telford, London*, 139–144.

Bayer, B., Simoni, A., Mulas, M., Corsini, A., & Schmidt, D. (2018). Deformation responses of slow moving landslides to seasonal rainfall in the Northern Apennines, measured by InSAR. *Geomorphology*, *308*, 293–306.

Bekaert, D. P., Karim, M., Linick, J. P., Hua, H., Sangha, S., Lucas, M., et al. (2019). Development of open-access Standardized InSAR Displacement Products by the Advanced Rapid Imaging and Analysis (ARIA) Project for Natural Hazards. In *AGU Fall Meeting Abstracts* (Vol. 2019, pp. G23A-04).

Bekaert, D. P., Handwerger, A. L., Agram, P., & Kirschbaum, D. B. (2020). InSAR-based detection method for mapping and monitoring slow-moving landslides in remote regions with steep and mountainous terrain: An application to Nepal. *Remote Sensing of Environment*, 249, 111983.

Bennett, G. L., Roering, J. J., Mackey, B. H., Handwerger, A. L., Schmidt, D. A., & Guillod, B. P. (2016). Historic drought puts the brakes on earthflows in Northern California. *Geophysical Research Letters*, *43*(11), 5725–5731.

Bennett, G. L., Miller, S. R., Roering, J. J., & Schmidt, D. A. (2016). Landslides, threshold slopes, and the survival of relict terrain in the wake of the Mendocino Triple Junction. *Geology*, *44*(5), 363–366.

Bhattacharya, P., & Viesca, R. C. (2019). Fluid-induced aseismic fault slip outpaces pore-fluid migration. *Science*, *364*(6439), 464–468.

Bogaard, T. A., & Greco, R. (2016). Landslide hydrology: from hydrology to pore pressure. *Wiley Interdisciplinary Reviews: Water*, *3*(3), 439–459.

Booth, A. M., McCarley, J. C., & Nelson, J. (2020). Multi-year, three-dimensional landslide surface deformation from repeat lidar and response to precipitation: Mill Gulch earthflow, California. *Landslides*, 1–14.

Buzzanga, B., Bekaert, D. P., Hamlington, B. D., & Sangha, S. S. (2020). Toward sustained monitoring of subsidence at the coast using insar and gps: An application in hampton roads, virginia. *Geophysical Research Letters*, *47*(18), e2020GL090013.

Calabro, M., Schmidt, D., & Roering, J. (2010). An examination of seasonal deformation at the Portuguese Bend landslide, southern California, using radar interferometry. *Journal of Geophysical Research: Earth Surface (2003–2012)*, *115*(F2).

Cappa, F., Scuderi, M. M., Collettini, C., Guglielmi, Y., & Avouac, J.-P. (2019). Stabilization of fault slip by fluid injection in the laboratory and in situ. *Science Advances*, *5*(3), eaau4065.

Carey, J. M., Massey, C. I., Lyndsell, B., & Petley, D. N. (2019). Displacement mechanisms of slow-moving landslides in response to changes in porewater pressure and dynamic stress. *Earth Surface Dynamics*, *7*(3), 707–722.

Carlà, T., Intrieri, E., Raspini, F., Bardi, F., Farina, P., Ferretti, A., et al. (2019). Perspectives on the prediction of catastrophic slope failures from satellite InSAR. *Scientific Reports*, *9*(1), 1–9.

Cicoira, A., Beutel, J., Faillettaz, J., & Vieli, A. (2019). Water controls the seasonal rhythm of rock glacier flow. *Earth and Planetary Science Letters*, *528*, 115844.

Cigna, F., & Tapete, D. (2021). Present-day land subsidence rates, surface faulting hazard and risk in Mexico City with 2014–2020 Sentinel-1 IW InSAR. *Remote Sensing of Environment*, *253*, 112161.

Coe, J. A., Ellis, W. L., Godt, J. W., Savage, W. Z., Savage, J. E., Michael, J., et al. (2003). Seasonal movement of the Slumgullion landslide determined from Global Positioning System surveys and field instrumentation, July 1998–March 2002. *Engineering Geology*, *68*(1), 67–101.

Cohen-Waeber, J., Bürgmann, R., Chaussard, E., Giannico, C., & Ferretti, A. (2018). Spatiotemporal Patterns of Precipitation-Modulated Landslide Deformation from Independent Component Analysis of InSAR Time Series. *Geophysical Research Letters*, 45(4), 1878-1887.

Corominas, J., Moya, J., Ledesma, A., Lloret, A., & Gili, J. A. (2005). Prediction of ground displacements and velocities from groundwater level changes at the Vallcebre landslide (Eastern Pyrenees, Spain). *Landslides*, 2(2), 83–96. https://doi.org/10.1007/s10346-005- 0049-1

Dehls, J. F., Larsen, Y., Marinkovic, P., Lauknes, T. R., Stødle, D., & Moldestad, D. A. (2019). INSAR. No: A National Insar Deformation Mapping/Monitoring Service In Norway--From Concept To Operations. In *IGARSS 2019-2019 IEEE International Geoscience and Remote Sensing Symposium* (pp. 5461–5464). IEEE.

Dille, A., Kervyn, F., Handwerger, A. L., d'Oreye, N., Derauw, D., Bibentyo, T. M., et al. (2021). When image correlation is needed: Unravelling the complex dynamics of a slow-moving landslide in the tropics with dense radar and optical time series. *Remote Sensing of Environment*, *258*, 112402.

Dong, L., Leung, L. R., Lu, J., & Gao, Y. (2019). Contributions of extreme and non-extreme precipitation to California precipitation seasonality changes under warming. *Geophysical Research Letters*, *46*(22), 13470–13478.

Efron, B., & Tibshirani, R. (1986). Bootstrap methods for standard errors, confidence intervals, and other measures of statistical accuracy. *Statistical Science*, 54–75.

Farr, T. G., Rosen, P. A., Caro, E., Crippen, R., Duren, R., Hensley, S., et al. (2007). The shuttle radar topography mission. *Reviews of Geophysics*, *45*(2).

Finnegan, N. J., Broudy, K. N., Nereson, A. L., Roering, J. J., Handwerger, A. L., & Bennett, G. (2019). River channel width controls blocking by slow-moving landslides in California's Franciscan mélange. *Earth Surface Dynamics*, *7*(3), 879–894.

Finnegan, N. J., Perkins, J. P., Nereson, A. L., & Handwerger, A. L. (2021). Unsaturated Flow Processes and the Onset of Seasonal Deformation in Slow-Moving Landslides. *Journal of Geophysical Research: Earth Surface*, *126*(5), e2020JF005758.

Gariano, S. L., & Guzzetti, F. (2016). Landslides in a changing climate. *Earth-Science Reviews*, *162*, 227–252.

Hahm, W. J., Rempe, D. M., Dralle, D. N., Dawson, T. E., Lovill, S. M., Bryk, A. B., et al. (2019). Lithologically controlled subsurface critical zone thickness and water storage capacity determine regional plant community composition. *Water Resources Research*, *55*(4), 3028–3055.

Handwerger, A. L., Roering, J. J., & Schmidt, D. A. (2013). Controls on the

seasonal deformation of slow-moving landslides. *Earth and Planetary Science Letters*, *377*, 239–247.

Handwerger, A. L., Huang, M.-H., Fielding, E. J., Booth, A. M., & Bürgmann, R. (2019). A shift from drought to extreme rainfall drives a stable landslide to catastrophic failure. *Scientific Reports*, *9*(1), 1569. https://doi.org/10.1038/s41598-018-38300-0

Handwerger, A. L., Fielding, E. J., Huang, M.-H., Bennett, G. L., Liang, C., & Schulz, W. H. (2019). Widespread initiation, reactivation, and acceleration of landslides in the northern California Coast Ranges due to extreme rainfall. *Journal of Geophysical Research: Earth Surface*, *124*(7), 1782–1797.

Hapke, C. J., & Green, K. R. (2006). Coastal landslide material loss rates associated with severe climatic events. *Geology*, *34*(12), 1077–1080.

Huang, M.-H., Fielding, E. J., Liang, C., Milillo, P., Bekaert, D., Dreger, D., & Salzer, J. (2017). Coseismic deformation and triggered landslides of the 2016 Mw 6.2 Amatrice earthquake in Italy. *Geophysical Research Letters*, *44*(3), 1266–1274.

Intrieri, E., Raspini, F., Fumagalli, A., Lu, P., Del Conte, S., Farina, P., et al. (2017). The Maoxian landslide as seen from space: detecting precursors of failure with Sentinel-1 data. *Landslides*.

Iverson, R. M. (2005). Regulation of landslide motion by dilatancy and pore pressure feedback. *Journal of Geophysical Research: Earth Surface*, *110*(F2).

Iverson, R. M., & Major, J. J. (1987). Rainfall, ground-water flow, and seasonal movement at Minor Creek landslide, northwestern California: Physical interpretation of empirical relations. *Geological Society of America Bulletin*, *99*(4), 579–594.

Iverson, R. M., George, D. L., Allstadt, K., Reid, M. E., Collins, B., Vallance, J. W., et al. (2015). Landslide mobility and hazards: Implications of the 2014 Oso disaster. *Earth and Planetary Science Letters*, *412*, 197–208.

Jacquemart, M., & Tiampo, K. (2021). Leveraging time series analysis of radar coherence and normalized difference vegetation index ratios to characterize pre-failure activity of the Mud Creek landslide, California. *Natural Hazards and Earth System Sciences*, *21*(2), 629–642.

Jennings, C. W., Gutierrez, C., Bryant, W., Saucedo, G., Wills, C. J., Milind, P., et al. (2010). Geologic Map of California. California Geological Survey, California Department of Conservation. Retrieved from https://cadoc.maps.arcgis.com/apps/mapviewer/index.html?layers=9eba56d981df4f839769ce9a2adc01f4

Jibson, R. W. (2006). The 2005 La Conchita, California, landslide. *Landslides*, *3*(1), 73–78.

Jones, J., Jones, C. E., & Bekaert, D. P. (2021). Value of InSAR for Monitoring Land Subsidence to Support Water Management in the San Joaquin Valley,

California. *Journal of the American Water Resources Association.* 1– 7

Keefer, D. K., & Johnson, A. M. (1983). Earth flows: morphology, mobilization, and movement.

Kelsey, H. M. (1978). Earthflows in Franciscan melange, Van Duzen River basin, California. *Geology*, *6*(6), 361–364.

Kenner, R., Phillips, M., Beutel, J., Hiller, M., Limpach, P., Pointner, E., & Volken, M. (2017). Factors controlling velocity variations at short-term, seasonal and multiyear time scales, Ritigraben rock glacier, Western Swiss Alps. *Permafrost and Periglacial Processes*, *28*(4), 675–684.

Kilburn, C. R., & Petley, D. N. (2003). Forecasting giant, catastrophic slope collapse: lessons from Vajont, Northern Italy. *Geomorphology*, *54*(1), 21–32.

Lacroix, P., Dehecq, A., & Taipe, E. (2020). Irrigation-triggered landslides in a Peruvian desert caused by modern intensive farming. *Nature Geoscience*, *13*(1), 56–60.

Lacroix, P., Handwerger, A. L., & Bièvre, G. (2020). Life and death of slow-moving landslides. *Nature Reviews Earth & Environment*, 1–16.

Lazecký, M., Spaans, K., González, P. J., Maghsoudi, Y., Morishita, Y., Albino, F., et al. (2020). LiCSAR: An automatic InSAR tool for measuring and monitoring tectonic and volcanic activity. *Remote Sensing*, *12*(15), 2430.

Liu, X., Zhao, C., Zhang, Q., Yin, Y., Lu, Z., Samsonov, S., et al. (2021). Three-dimensional and long-term landslide displacement estimation by fusing C- and L-band SAR observations: A case study in Gongjue County, Tibet, China. *Remote Sensing of Environment*, *267*, 112745.

Lundgren, P., Girona, T., Bato, M. G., Realmuto, V. J., Samsonov, S., Cardona, C., et al. (2020). The dynamics of large silicic systems from satellite remote sensing observations: The intriguing case of Domuyo volcano, Argentina. *Scientific Reports*, *10*(1), 1–15.

Mackey, B. H., & Roering, J. J. (2011). Sediment yield, spatial characteristics, and the long-term evolution of active earthflows determined from airborne LiDAR and historical aerial photographs, Eel River, California. *Geological Society of America Bulletin*, *123*(7–8), 1560–1576.

Mackey, B. H., Roering, J. J., & McKean, J. (2009). Long-term kinematics and sediment flux of an active earthflow, Eel River, California. *Geology*, *37*(9), 803–806.

Malet, J.-P., Maquaire, O., & Calais, E. (2002). The use of Global Positioning System techniques for the continuous monitoring of landslides: application to the Super-Sauze earthflow (Alpes-de-Haute-Provence, France). *Geomorphology*, *43*(1), 33–54.

Matsuura, S., Asano, S., & Okamoto, T. (2008). Relationship between rain and/or meltwater, pore-water pressure and displacement of a reactivated landslide. *Engineering Geology*, *101*(1–2), 49–59.

McSaveney, M. J., & Griffiths, G. A. (1987). Drought, rain, and movement of a recurrent earthflow complex in New Zealand. *Geology*, *15*(7), 643–646.

Merriam, R. (1960). Portuguese Bend landslide, Palos Verdes Hills, California. *The Journal of Geology*, *68*(2), 140–153.

Milillo, P., Sacco, G., Martire, D. D., & Hua, H. (2021). Neural-network pattern recognition experiments toward a full-automatic detection of anomalies in InSAR time-series of surface deformation. *Frontiers in Earth Science*, 1132.

Minchew, B. M., & Meyer, C. R. (2020). Dilation of subglacial sediment governs incipient surge motion in glaciers with deformable beds. *Proc. R. Soc. A.*, *476*(2238). https://doi.org/10.1098/rspa.2020.0033

Moon, T., Joughin, I., Smith, B., Van Den Broeke, M. R., Van De Berg, W. J., Noël, B., & Usher, M. (2014). Distinct patterns of seasonal Greenland glacier velocity. *Geophysical Research Letters*, *41*(20), 7209–7216.

Morishita, Y., Lazecky, M., Wright, T. J., Weiss, J. R., Elliott, J. R., & Hooper, A. (2020). LiCSBAS: an open-source InSAR time series analysis package integrated with the LiCSAR automated Sentinel-1 InSAR processor. *Remote Sensing*, *12*(3), 424.

Nereson, A. L., & Finnegan, N. J. (2018). Drivers of earthflow motion revealed by an 80 yr record of displacement from Oak Ridge earthflow, Diablo Range, California, USA. *Geological Society of America Bulletin*.

Nereson, A. L., Davila Olivera, S., & Finnegan, N. J. (2018). Field and Remote-Sensing Evidence for Hydro-mechanical Isolation of a Long-Lived Earthflow in Central California. *Geophysical Research Letters*, *45*(18), 9672–9680.

Polade, S. D., Gershunov, A., Cayan, D. R., Dettinger, M. D., & Pierce, D. W. (2017). Precipitation in a warming world: Assessing projected hydro-climate changes in California and other Mediterranean climate regions. *Scientific Reports*, *7*(1), 1–10.

Raspini, F., Bianchini, S., Ciampalini, A., Del Soldato, M., Solari, L., Novali, F., et al. (2018). Continuous, semi-automatic monitoring of ground deformation using Sentinel-1 satellites. *Scientific Reports*, *8*(1), 1–11.

Robeson, S. M. (2015). Revisiting the recent California drought as an extreme value. *Geophysical Research Letters*, *42*(16), 6771–6779.

Rosen, P. A., Gurrola, E., Sacco, G. F., & Zebker, H. (2012). The InSAR scientific computing environment. In *Synthetic Aperture Radar, 2012. EUSAR. 9th European Conference on* (pp. 730–733).

Rutter, E., & Green, S. (2011). Quantifying creep behaviour of clay-bearing rocks below the critical stress state for rapid failure: Mam Tor landslide, Derbyshire, England. *Journal of the Geological Society*, *168*(2), 359–372.

Scheingross, J. S., Minchew, B. M., Mackey, B. H., Simons, M., Lamb, M. P., & Hensley, S. (2013). Fault-zone controls on the spatial distribution of slow-moving landslides. *Geological Society of America Bulletin*, *125*(3–4), 473–489.

Schulz, W. H., Smith, J. B., Wang, G., Jiang, Y., & Roering, J. J. (2018). Clayey landslide initiation and acceleration strongly modulated by soil swelling. *Geophysical Research Letters*, *45*(4), 1888–1896.

Shugar, D. H., Jacquemart, M., Shean, D., Bhushan, S., Upadhyay, K., Sattar, A., et al. (2021). A massive rock and ice avalanche caused the 2021 disaster at Chamoli, Indian Himalaya. *Science*, *373*(6552), 300–306.

Strozzi, T., Caduff, R., Jones, N., Barboux, C., Delaloye, R., Bodin, X., et al. (2020). Monitoring rock glacier kinematics with satellite synthetic aperture radar. *Remote Sensing*, *12*(3), 559.

Swain, D. L., Tsiang, M., Haugen, M., Singh, D., Charland, A., Rajaratnam, B., & Diffenbaugh, N. S. (2014). The extraordinary California drought of 2013/2014: Character, context, and the role of climate change. *Bulletin of the American Meteorological Society*, *95*(9), S3.

Swain, D. L., Langenbrunner, B., Neelin, J. D., & Hall, A. (2018). Increasing precipitation volatility in twenty-first-century California. *Nature Climate Change*, 1.

Swirad, Z. M., & Young, A. P. (2021). Automating coastal cliff erosion measurements from large-area LiDAR datasets in California, USA. *Geomorphology*, 107799.

Terzaghi, K. (1951). *Mechanism of Landslides*. Harvard University, Department of Engineering.

Wang, S.-Y. S., Yoon, J.-H., Becker, E., & Gillies, R. (2017). California from drought to deluge. *Nature Climate Change*, *7*(7), 465–468.

Warrick, J. A., Ritchie, A. C., Schmidt, K. M., Reid, M. E., & Logan, J. (2019). Characterizing the catastrophic 2017 Mud Creek landslide, California, using repeat structure-from-motion (SfM) photogrammetry. *Landslides*, 1–19.

Wills, C. J., Manson, M. W., Brown, K. D., Davenport, C. W., & Domrose, C. J. (2001). Landslides in the Highway 1 Corridor: Geology and Slope Stability along the Big Sur Coast between Point Lobos and San Carpoforo Creek, Monterey and San Luis Obispo Counties, California. *California Department of Transportation Project F99TL34*.

Wills, C. J., Roth, N. E., McCrink, T. P., Short, W. R., DeGraff, J., & Shakoor, A. (2017). The California landslide inventory database. In *Proc. Third North*

American Symp. on Landslides, Roanoke, VA, Association of Environmental and Engineering Geologists (pp. 666–674).

Xu, Y., Schulz, W. H., Lu, Z., Kim, J., & Baxtrom, K. (2021). Geologic controls of slow-moving landslides near the US West Coast. *Landslides*, 1–13.

Young, A. P. (2015). Recent deep-seated coastal landsliding at San Onofre State Beach, California. *Geomorphology*, *228*, 200–212.

Yunjun, Z., Fattahi, H., & Amelung, F. (2019). Small baseline InSAR time series analysis: Unwrapping error correction and noise reduction. *Computers & Geosciences*, *133*, 104331. https://doi.org/10.1016/j.cageo.2019.104331

References From the Supporting Information

Fattahi, H., & Amelung, F. (2013). DEM error correction in InSAR time series. IEEE Transactions on Geoscience and Remote Sensing, 51(7), 4249-4259.

Handwerger, A. L., Booth, A. M., Huang, M. H., & Fielding, E. J. (2021). Inferring the Subsurface Geometry and Strength of Slow-Moving Landslides Using 3-D Velocity Measurements From the NASA/JPL UAVSAR. *Journal of Geophysical Research: Earth Surface*, 126(3), e2020JF005898.

Jolivet, R., Grandin, R., Lasserre, C., Doin, M. P., & Peltzer, G. (2011). Systematic InSAR tropospheric phase delay corrections from global meteorological reanalysis data. Geophysical Research Letters, 38(17).

Liu, L., Millar, C. I., Westfall, R. D., & Zebker, H. A. (2013). Surface motion of active rock glaciers in the Sierra Nevada, California, USA: inventory and a case study using InSAR. *The Cryosphere*, 7(4), 1109-1119.

Geophysical Research Letters

Supporting Information for

Landslide Sensitivity and Response to Precipitation Changes in Wet and Dry Climates

Alexander L. Handwerger[1,2], Eric J. Fielding[1], Simran S. Sangha[1,3], and David P.S. Bekaert[1]

[1]Jet Propulsion Laboratory, California Institute of Technology, Pasadena, USA. [2]Joint Institute for Regional Earth System Science and Engineering, University of California, Los Angeles, Los Angeles, USA. [3]Earth, Planetary, and Space Sciences, University of California, Los Angeles, CA, USA.

Contents of this file

Additional Supporting Information (Files uploaded separately)

Text S1.

InSAR Processing and Analyses

JPL-Caltech ARIA automatically processed standardized interferograms with Sentinel-1 data between 2015 and 2021 for California. At the time this study was performed however the InSAR data were only processed up to early 2020 (Figures 2 and 3). ARIA produced interferograms with 3 nearest connected neighbors and year-long pairs. We used the ARIA-tools open-source package in Python (https://github.com/aria-tools) to download all of the interferograms covering California. We downloaded 13825 individual products which was equivalent to 1689 merged interferograms from ascending tracks 35, 64, and 137, and descending tracks 42, 71, 115, 144, 173 (the full list of the InSAR data used in this study are in Table S1). The ARIA-tools package combines adjacent products into merged interferograms. We found there were sometimes discontinuities in the merged interferograms that resulted during unwrapping between data frames. Interferograms containing discontinuities were manually identified and removed from our analyses for the landslide identification stage, but were included for the time series analyses of selected landslides because the individual landslides did not span these discontinuities.

In order to search for landslides, it is important to use local reference points to help further reduce long wavelength noise that can obscure the landslide signal. We selected 32 regional stable (i.e., no motion) reference points that were used to reset the InSAR data velocity values (Table S4) and facilitate landslide detection. Additionally, we removed noise by excluding pixels with coherence less than 0.4, and applied linear deramping, DEM error correction (Fattahi & Amelung, 2013), and tropospheric corrections (Jolivet et al., 2011) with the European Centre for Medium-Range Weather Forecasts (ECMWF) ERA-5 reanalysis data set.

Once we selected the 38 landslides for time series analyses, we subset both ascending and descending InSAR data for each landslide and reprocessed the time series using a new local stable reference point. We then selected either ascending or descending data, depending on which data showed the best quality landslide signal (Figure S2). Finally, we projected the line-of-sight time series onto the mean downslope direction of each landslide, assuming surface-parallel motion using:

$$D_{downslope} = \frac{D_{LOS}}{sin(\alpha - \beta)sin(\theta_{inc})sin(\theta_{slp}) + cos(\theta_{inc})sin(\theta_{slp})}$$

where α is the heading direction (in degrees, positive counterclockwise from north) of the radar platform in the horizontal plane, θ_{inc} is the incidence angle, β is the mean azimuth angle of the landslide (i.e., downslope direction heading) and θ_{slp} is the mean hillslope angle of the landslide (Liu et al., 2013). This downslope projection can provide more accurate estimates of the true landslide displacement magnitude.

Landslide Classification and Geometric Scaling

We classified landslide types as slumps, earthflows, and complexes. We used the classification from Handwerger et al. (2021) where "slumps are landslides with lower length/width aspect ratios and one primary kinematic zone. Earthflows are landslides with medium aspect ratios and one primary kinematic zone. And landslide complexes are landslides with higher aspect ratios that are composed of multiple kinematic zones or even multiple landslides that coalesce into a single landslide mass".

We estimated landslide thickness using geometric scaling relations developed for slow-moving landslides in California (Handwerger et al., 2021). Landslide scaling relations take the form of a power function defined as

$$V = c_V A^{\gamma} \text{ and } h = c_h A^{\zeta}$$

where γ and ζ are the scaling exponents and c_V and c_h are fit intercepts. See parameters in Table (S5)

Supplementary Figures

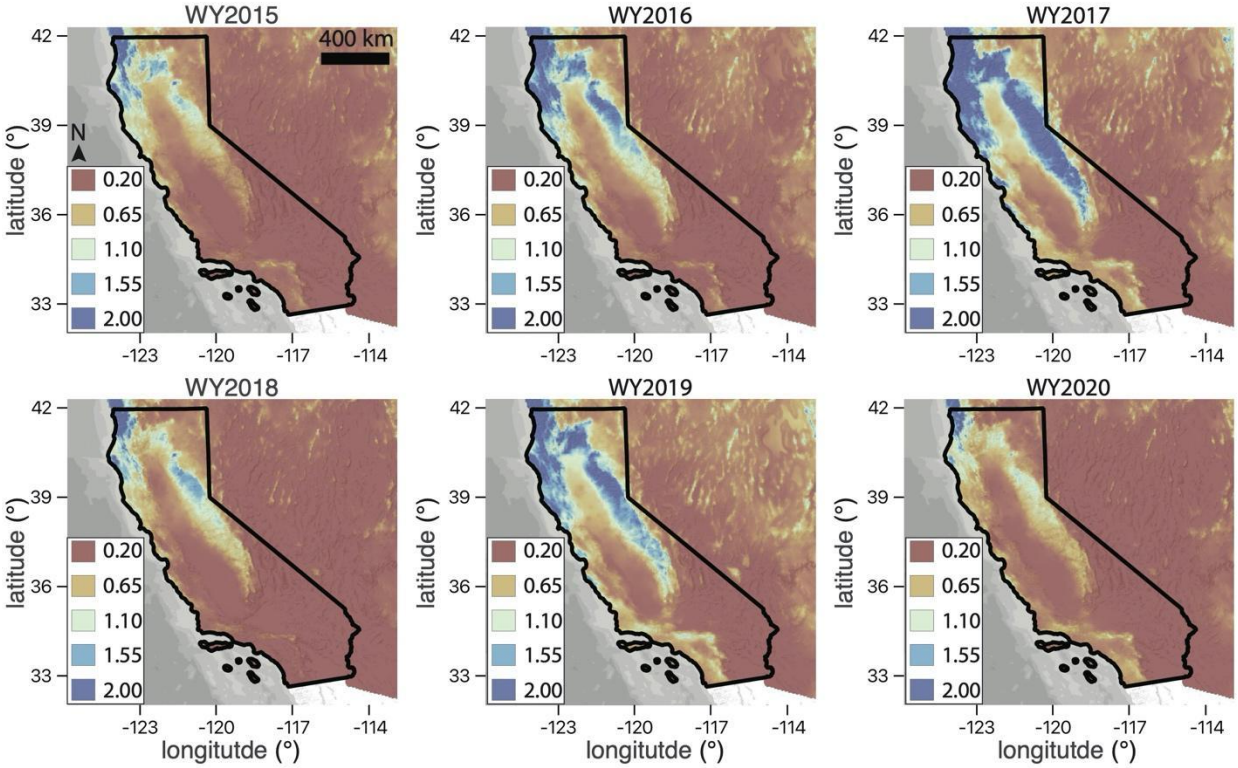

Figure S1. Water year precipitation maps. Colors show the total water year precipitation (m/yr). Data are from PRISM.

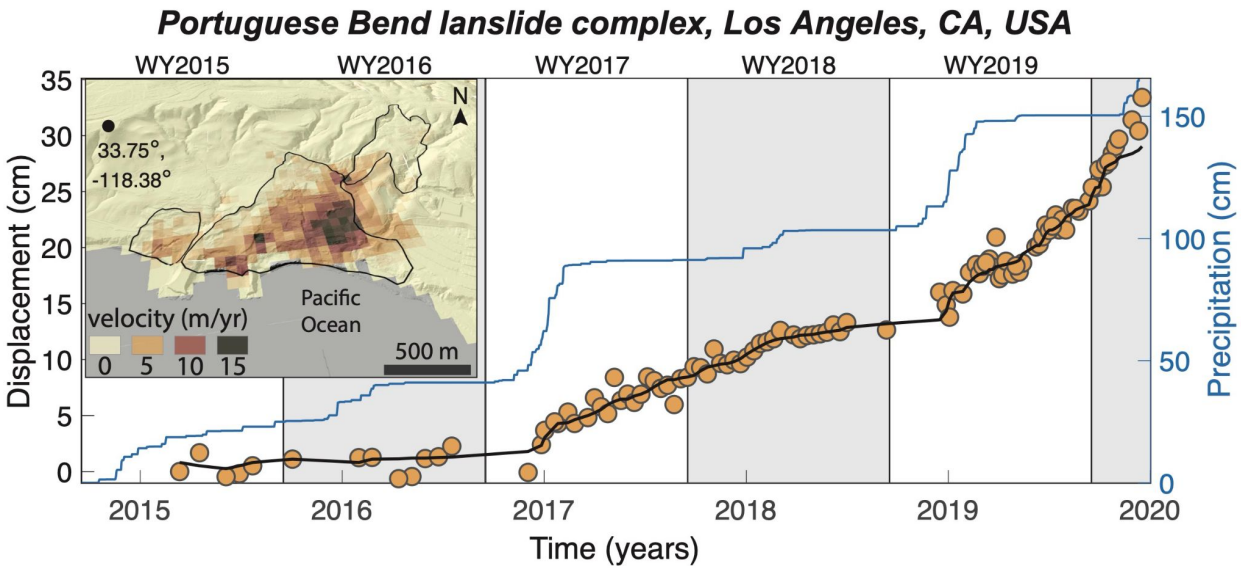

Figure S2. Displacement and precipitation time series for Portuguese Bend landslide. Orange circles show raw InSAR time series and black line shows smoothed time series. Displacement data are projected onto the downslope direction. Blue line shows cumulative precipitation time series. Inset shows oblique view of InSAR velocity map draped over a lidar hillshade. Black circle shows the location of the reference point for the time series and black polygons show active landslide boundaries.

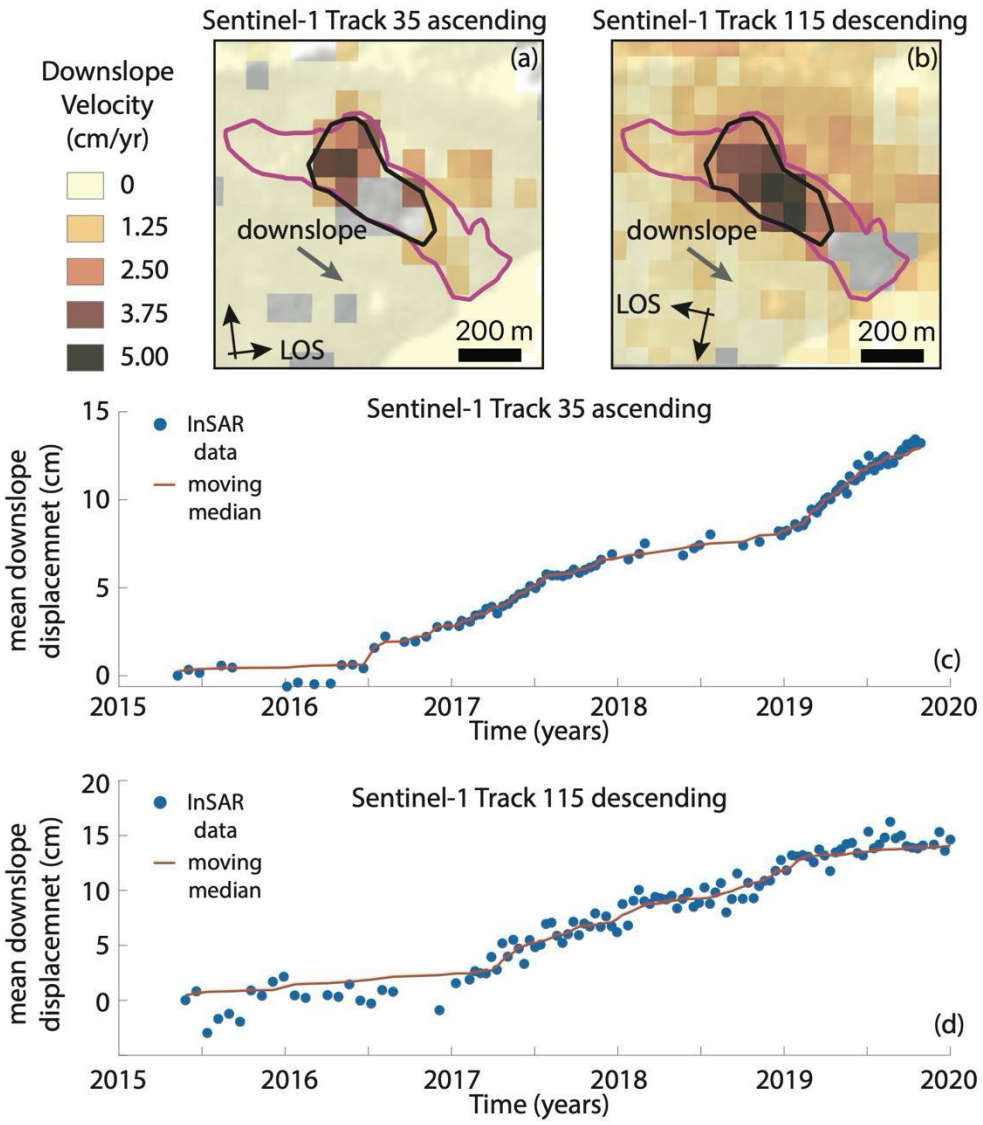

Figure S3. Example ascending and descending deformation maps and time series for a single landslide. (a-b) InSAR velocity maps draped over a hillshade of topography. Red colors show relatively high velocities. Magenta polygon shows the extent of the geomorphic landslide. Black polygon shows the fastest moving zone used to calculate the mean displacement plotted in (c-d). Arrows show downslope direction of landslide, satellite line-of-sight (LOS), and satellite flight heading. (c-d) Mean downslope displacement time series for ascending and descending InSAR data. Blue circles show the raw InSAR data and the orange line shows moving median smoothed time series.

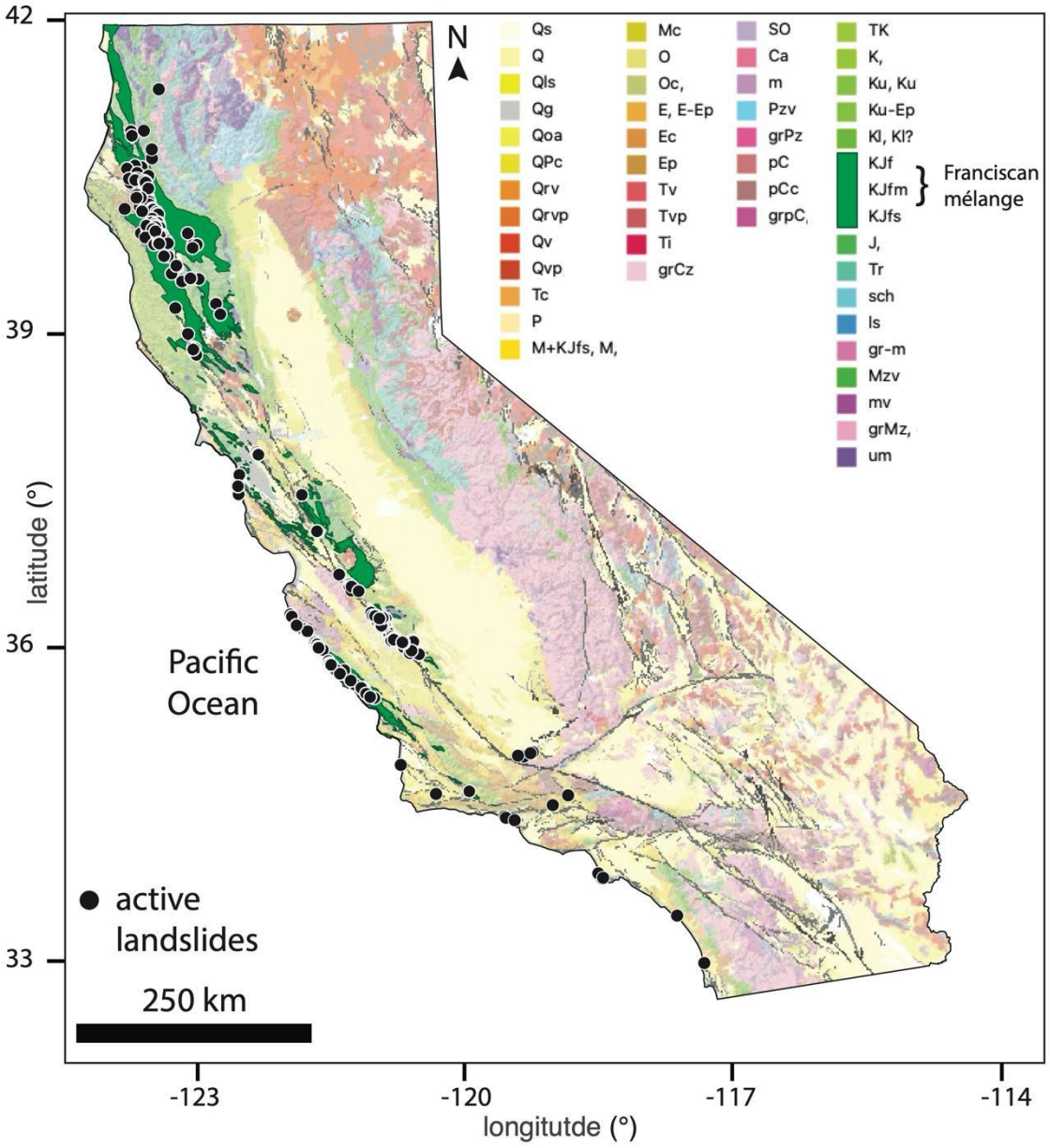

Figure S4. Geologic map of California. Black circles show location of active landslides identified with InSAR data. Data are provided by the California Geologic Survey. For detailed rock type descriptions see list at: https://maps.conservation.ca.gov/cgs/metadata/GDM_002_GMC_750k_v2_metadata.html.

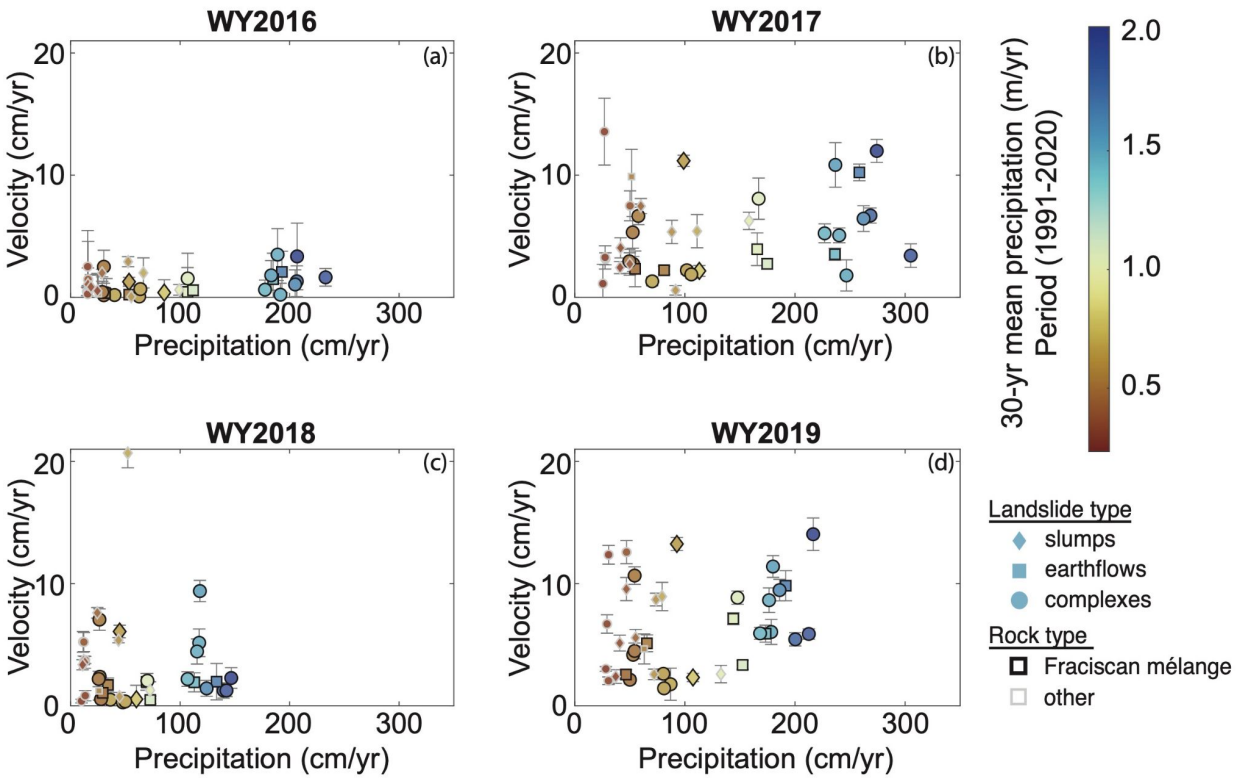

Figure S5. Landslide kinematics in response to changes in precipitation. (a-d) Water year (WY) velocity as a function of WY precipitation for selected landslides. Error bars show the uncertainty in the velocity estimates. Red to blue colors correspond to the 30 year normal precipitation (1991-2020) for each landslide. Symbols correspond to landslide type. Rock type is shown by black or gray symbol border color.

Supplementary Tables

Table S1. List of all InSAR pairs used in study. Columns correspond to the reference acquisition dates, secondary acquisition dates, perpendicular baseline, the timespan between images, and the total number of interferograms used in the time series inversion. The file contains eight spreadsheets that correspond to different satellite track numbers.

Table S2. Landslide inventory data table. Table includes information for landslide type, host rock type, mean slope angle, landslide area, landslide length, landslide width, centroid location of each landslide, and 30-year mean water year precipitation for each landslide (WY1990-WY2019).

Table S3. Landslide data table for the 38 selected landslides. Table includes information for landslide name, centroid location, landslide type, host rock type, landslide area, landslide length, landslide width, estimated landslide volume, estimated landslide thickness, mean slope angle, downslope aspect direction, InSAR data used for final time series analyses, stable reference point, and velocity and precipitation data.

reference point longitude (degrees)	reference point latitude (degrees)
-116.3914054	34.26675748
-116.5356684	33.8258261
-117.274774	32.844484
-117.646708	34.288767
-117.8200602	33.62590427
-118.3619388	33.76003981
-118.575646	34.042921
-118.67185	34.55515674
-119.632258	37.985456
-120.0213188	39.4384228
-120.021619	39.43817
-120.87114	36.272458
-121.0954394	36.74856042
-121.190797	36.622521
-121.445966	35.876472
-121.536581	36.026733
-121.585882	36.061785
-121.675278	37.344674
-121.7488595	37.46076441
-121.809952	36.26085
-121.8681335	37.15969
-121.886534	36.426898
-122.265977	37.31953
-122.290836	37.926315
-122.483311	37.699138
-123.050031	38.885312
-123.3293693	39.65829982
-123.393747	39.806784
-123.467188	40.106911
-123.800918	40.558561
-123.816244	40.987106

Table S4. Location of stable reference points used for landslide identification during the statewide mapping.

category	c_v, best fit intercept	γ, best fit power function exponent	c_b, best fit intercept	ζ, best fit power function exponent
inventory	0.2074 (0.0746, 0.5761)	1.306 (1.213, 1.399)	0.2074 (0.0746, 0.5761)	0.3058 (0.2129, 0.3987)
slumps	0.0301 (0.0020, 0.4569)	1.493 (1.224, 1.762)	0.0301 (0.0020, 0.4569)	0.4926 (0.2236, 0.7615)
earthflows	0.0207 (0.0013, 0.3389)	1.535 (1.273, 1.796)	0.0207 (0.0013, 0.3389)	0.5348 (0.2734, 0.7963)
complexes	0.9542 (0.1029, 1.2674)	1.172 (0.9858, 1.357)	0.9542 (0.1029, 1.2674)	0.1716 (-0.0142, 0.3573)

Table S5. Volume-area scaling fit values (with 95% confidence bounds). Table is modified from Handwerger et al., 2021.